https://doi.org/10.5194/egusphere-2026-597
Preprint. Discussion started: 23 February 2026
© Author(s) 2026. CC BY 4.0 License.

Impacts of ridge-induced upwelling on the biological carbon pump in the tropical Northwestern Pacific

Shujin Guo[1, 2, 3†], Mingliang Zhu[2, 4†], Shan Zheng[1, 2, 3], Wenlong Xu[5], Jinming Song[1], Yongfang Zhao[2], Sheng Dai[6], Junhua Liang[2], Chenhao Zhao[7], Xiaoxia Sun[1, 2, 3]

[1]Laboratory of Marine Ecology and Environmental Sciences, Shandong Province Key Laboratory of Marine Biodiversity and Bio-resource Sustainable Utilization, Institute of Oceanology, Chinese Academy of Sciences, Qingdao 266071, China

[2]Jiaozhou Bay National Marine Ecosystem Research Station, Institute of Oceanology, Chinese Academy of Sciences, Qingdao 266071, China

[3]Laboratory for Marine Ecology and Environmental Science, Qingdao Marine Science and Technology Center, Qingdao 266237, China

[4]University of Chinese Academy of Sciences, Beijing 100049, China

[5]Ocean College, Jiangsu University of Science and Technology, Zhenjiang 212100, China

[6]Key Laboratory of Tropical Marine Bio-resources and Ecology, Guangdong Provincial Key Laboratory of Applied Marine Biology, South China Sea Institute of Oceanology, Chinese Academy of Sciences, Guangzhou 510301, China

[7]Shanghai Fisheries Research Institute, Shanghai Fisheries Technical Extension Station, Shanghai 200433, China

Correspondence to: Xiaoxia Sun (xsun@qdio.ac.cn)

Abstract. Submarine ridges are prominent topographic features in the global ocean, yet their role in regulating the biological carbon pump remains underexplored. In this study, we investigated the spatial variability of phytoplankton production, particle dynamics, and carbon export along a meridional transect in the tropical Northwestern Pacific, spanning a warm eddy (WE), a cold eddy (CE), and the Kyushu-Palau Ridge (KPR). A suite of *in situ* measurements, including ^{14}C-based primary production, HPLC pigment analysis, and particle profiling via Underwater Vision Profiler (UVP5-HD), was used to assess regional differences in biological carbon pump processes. Marked thermocline shoaling and nutrient uplift were observed in both the CE and KPR regions, but the KPR-derived upwelling waters had higher nutrient concentrations, resulting in the highest nutrient inventories in the upper 200 m and supporting elevated primary production (142.05 mg C m^{-2} d^{-1}) and phytoplankton biomass there.

† These authors contributed equally to this work.

https://doi.org/10.5194/egusphere-2026-597
Preprint. Discussion started: 23 February 2026
© Author(s) 2026. CC BY 4.0 License.

Correspondingly, the KPR region exhibited the highest particle volume concentrations in the upper 200 m, followed by the CE, with the WE and background regions showing the lowest values. The 0–2000 m water column in the KPR region was also characterized by a substantially greater contribution of large particles (ESD ≥ 500 μm), which in turn supported enhanced particulate organic carbon (POC) export in this area. POC fluxes in the KPR region reached 9.04 ± 6.74, 5.52 ± 0.10, and 3.09 ± 1.96 mg C m^{-2} d^{-1} at 200 m, 1000 m, and 2000 m, respectively, which were 2.8 to 5.7 times higher than those in the CE region and 5.9 to 11.4 times higher than in the background region. Consistently, export efficiency (e-ratio) peaked in the KPR region (10%), exceeding those in the CE (3%), WE (3%), and background (5%) regions. Using the KPR as a representative case, our results highlight the critical role of ridge-induced upwelling in regulating phytoplankton production and particle dynamics, as well as enhancing biological carbon export and surface–deep coupling in oligotrophic oceans. These findings underscore the importance of incorporating such topographic processes into global oceanic carbon cycle research.

Key words: Kyushu-Palau Ridge (KPR), upwelling; phytoplankton productivity; particulate organic carbon (POC) flux, biological carbon pump, Underwater Vision Profiler (UVP), tropical Northwestern Pacific

1 Introduction

The biological carbon pump (BCP) comprises a suite of oceanic processes that together drive the continuous net uptake of atmospheric CO_2. Through photosynthesis in the sunlit surface ocean, phytoplankton convert dissolved inorganic carbon into organic matter at a global rate of approximately 50 GtC yr^{-1}, a fraction of which sinks as particulate organic carbon (POC) into the ocean interior (DeVries et al., 2012). Once transported below the mesopelagic zone (~1000 m), this POC becomes effectively isolated from the atmosphere for centuries or longer (Kwon et al., 2009). Without the operation of the BCP, atmospheric CO_2 concentrations would be about 200 ppm higher than today (Henson et al., 2019), indicating that the BCP plays a crucial role in mitigating global greenhouse effects. Furthermore, the downward flux of biogenic particles provides an important food source for deep-sea organisms (Rodil et al., 2020; Ramondenc et al., 2025). Several studies have confirmed that episodic or sustained pulses of sinking POC are critical for supporting deep-sea benthic food webs

https://doi.org/10.5194/egusphere-2026-597
Preprint. Discussion started: 23 February 2026
© Author(s) 2026. CC BY 4.0 License.

(Dunlop et al., 2016; Iversen, 2023). Therefore, the BCP is also essential for sustaining deep-sea ecosystems through the continuous supply of sinking organic carbon. The efficiency of the BCP, which is defined as the proportion of primary production exported from the euphotic zone and the fraction of this export that reaches the deep ocean, is modulated by a complex interplay of biological, physical, and chemical processes (Nowicki et al., 2022; Bressac et al., 2024; Visser, 2025). These include primary production and the formation of organic carbon, the formation, aggregation, and disaggregation of organic-rich particles; the attachment of organic matter to mineral ballast; zooplankton grazing and fecal pellet production; the sinking of organic carbon, and microbial remineralization (DeVries et al., 2012; Iversen, 2023; Siegel et al., 2023). Variations in these mechanisms across different oceanic regimes determine how effectively the surface ocean sequesters carbon at depth (De La Rocha and Passow, 2007; Louchard et al., 2021; Zhang et al., 2023).

Mid-ocean ridges are among the most prominent geomorphological features on Earth, forming a nearly continuous mountain chain that extends for over 60,000 km across the global ocean floor (Macdonald, 2001; Searle, 2013). Characterized by rugged topography, rift valleys, and steep flanks, ridge systems not only play a central role in plate tectonics and crustal formation but also exert strong influences on regional ocean dynamics across different basins (Searle, 2013). For instance, the Sulu Ridge in the southeastern South China Sea hosts a persistent upwelling and frontal system driven by strong internal tidal mixing (Jing et al., 2012; Dang et al., 2020). Intense vertical shear generated by tide-topography interactions enhances diapycnal mixing, resulting in a localized but persistent upward flux of deep waters. In the southern tropical Indian Ocean, the Seychelles–Chagos Thermocline Ridge represents the largest and most persistent upwelling system in the basin, where wind-driven Ekman divergence and thermocline doming sustain year-round upward water movement (Vinayachandran et al., 2021). Similarly, in the North Atlantic, the Mid-Atlantic Ridge profoundly shapes basin-scale circulation and hydrographic front positions through its control on flow pathways and mixing processes (Murphy et al., 2021). These studies have revealed the widespread and diverse impacts of ridge systems on vertical water exchange in the ocean. While it is well established that the strength and efficiency of the BCP are influenced by physical dynamics and water mass circulation, the potential effects of ridge-induced upwelling on the BCP remain largely unknown. Considering the vast area occupied by ridge systems across the global ocean (Searle, 2013), this lack of understanding hampers our ability to

https://doi.org/10.5194/egusphere-2026-597
Preprint. Discussion started: 23 February 2026
© Author(s) 2026. CC BY 4.0 License.

accurately assess global carbon export fluxes and biological pump efficiency.

The tropical Northwestern Pacific is a nutrient-deficient region characterized by persistently low Chl *a* concentrations and weak seasonal variability (Shih et al., 2015; Matsumoto et al., 2016). Primary productivity is generally low here, and picophytoplankton dominate the phytoplankton community in this oligotrophic environment (Zhang et al., 2023; An et al., 2024). The Kyushu–Palau Ridge (KPR) is one of the most prominent topographic features in this region. It extends for approximately 620 km, with a width of 46–148 km, covering an area of about 5.1×10^4 km^2 (Qin et al., 2021). The ridge divides the Philippine Sea into two parts: the West Philippine Basin to the west and the Parece Vela Basin to the east, with water depths ranging from 522 to 6234 m. The KPR has recently been identified as a major hotspot for deep diapycnal upwelling (Xiao et al., 2023; Song et al., 2024). High-resolution hydrographic observations revealed that enhanced turbulent mixing over the KPR plays a pivotal role in transforming and uplifting deep water masses, particularly the Lower Circumpolar Deep Water (LCDW) entering the Philippine Sea through the Yap–Mariana Junction (YMJ) (Zhou et al., 2022). This mixing is primarily driven by the breaking of high-mode internal tides generated by the rough KPR topography, with additional contributions from energetic lee waves and bottom currents (Song et al., 2024). Although the ridge accounts for only 21% of the deep Philippine Sea at 4000 m, it contributes 47% of the total diapycnal upwelling volume (Xiao et al., 2023), underscoring its disproportionate influence on regional overturning circulation. Such processes are not only crucial for regulating the physical properties of water masses but may also exert significant impacts on biogeochemical cycles in the overlying water column. However, the effects of KPR-induced upwelling on local carbon export processes and the efficiency of the biological carbon pump have not yet been investigated. This knowledge gap hampers a comprehensive understanding of carbon sequestration efficiency and its regulating mechanisms in the tropical Northwestern Pacific.

In this study, we conducted a northwest–southeast transect survey across the tropical Northwestern Pacific, crossing the KPR in December 2015. During the cruise, a warm eddy and a cold eddy were also observed, providing an excellent opportunity to compare the effects of eddy induced versus topography induced physical forcing on biological carbon pump processes. Hydrographic, biogeochemical, and biological measurements were obtained, including nutrient concentrations, primary productivity, phytoplankton community composition, particle size spectra, and POC fluxes,

https://doi.org/10.5194/egusphere-2026-597
Preprint. Discussion started: 23 February 2026
© Author(s) 2026. CC BY 4.0 License.

from which the efficiency of the biological carbon pump was derived. This study addresses two key questions: (1) Does the KPR influence upper-ocean carbon export processes, and what mechanisms drive this influence? (2) What are the differences in the effects of KPR-induced upwelling and mesoscale eddies on upper-ocean carbon export? By answering these questions, we aim to clarify the carbon export dynamics in the tropical Northwestern Pacific, an oligotrophic region traditionally regarded as an "oceanic desert" with a weak biological carbon pump, and to provide insights into how ridge-related physical processes may regulate carbon cycling in other ocean basins.

2 Material and methods

2.1 Study area and cruise overview

A research cruise was conducted in the tropical Northwestern Pacific from 11 to 22 December 2015 aboard the R/V *Kexue* (Fig. 1a). A total of nine sampling stations were distributed along a northwest–southeast transect spanning approximately 1300 km, covering latitudes from 11ºN to 21ºN and longitudes from 126ºE to 136ºE (Fig. 1b). The sampling transect extended from the western Philippine Basin to the Kyushu–Palau Ridge in the tropical Western Pacific. Detailed information on station coordinates and depths is provided in Table 1. Most stations were located in the abyssal plain, with bottom depths exceeding 5000 m. Exceptions were stations D11 and D12, which were situated on the Kyushu-Palau Ridge, a prominent bathymetric feature in the region, where the seafloor depths were 3826 m and 4740 m, respectively. At each station, an Underwater Vision Profiler (UVP 5.0) was deployed to a depth of 2000 m to capture vertical profiles of particle size and abundance distributions.

To characterize the hydrographic and dynamic conditions of the study area, satellite altimetry data were used to assess the spatial and temporal variability in sea surface height. Mesoscale eddies were identified as local extrema in sea level anomaly (SLA), with cyclonic eddies corresponding to SLA minima and anticyclonic eddies to SLA maxima. SLA fields were obtained from a multi-sensor gridded altimetry product distributed by the Copernicus Marine Environment Monitoring Service (product ID: SEALEVEL_GLO_PHY_CLIMATE_L4_MY_008_057). Based on satellite-derived SLA data (Fig. 1c), mesoscale eddies were active across the transect during the cruise period. Station D1 was located within an warm eddy core, characterized by a positive SLA of approximately +0.2 m. In contrast, stations D7, D8 and D9 were situated within a pronounced cold eddy, where SLA reached a minimum of approximately –0.3 m. Based on the SLA field and the bathymetric features, the transect

https://doi.org/10.5194/egusphere-2026-597
Preprint. Discussion started: 23 February 2026
© Author(s) 2026. CC BY 4.0 License.

was divided into four regions: (1) Warm eddy region (WE): represented by station D1, which was located at the periphery of an anticyclonic eddy; (2) Background region (BR): represented by stations D3, D4 and D5, situated in the western Philippine Basin where no strong eddy influence was apparent, thus reflecting background basin conditions; (3) Cold eddy region (CE): including stations D7, D8, and D9, which were located within a cyclonic eddy associated with negative sea surface height anomalies; (4) Kyushu-Palau Ridge region (KPR): represented by stations D11 and D12, positioned directly above the crest of the Kyushu-Palau Ridge, characterized by bottom depths of 3826 and 4740 m, which are substantially shallower than the abyssal plain at other stations (Table 1).

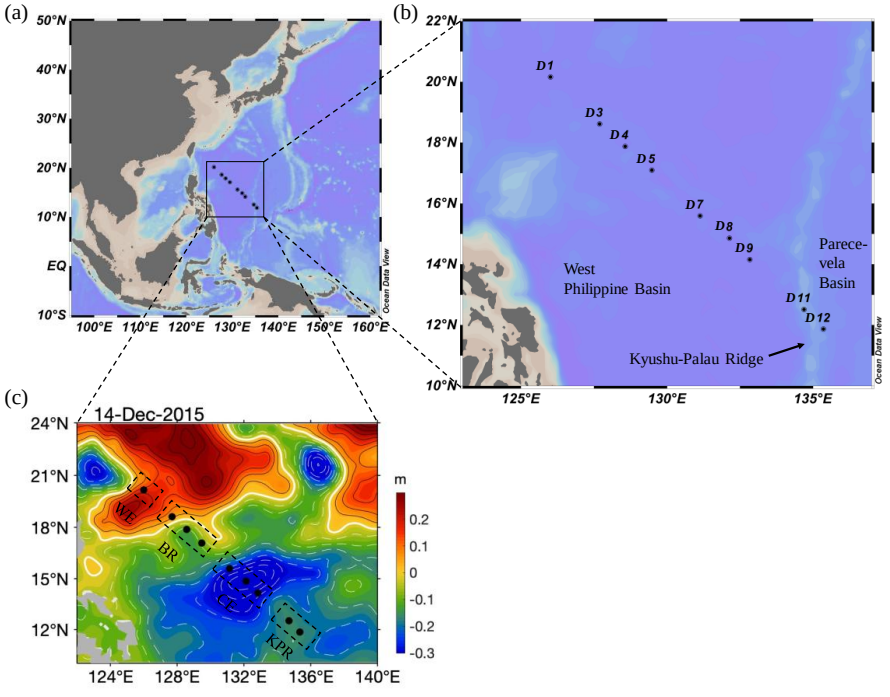

Fig. 1 Study area and survey stations in the tropical Northwestern Pacific. a: the study region; b: the enlarge view; c: sea level anomalies (SLA). The dots indicate the locations of the sampling stations. WE: warm eddy region; BR: background region; CE: cold eddy region; KPR: Kyushu–Palau Ridge region.

https://doi.org/10.5194/egusphere-2026-597
Preprint. Discussion started: 23 February 2026
© Author(s) 2026. CC BY 4.0 License.

Table 1. Location and deployment times of UVP in the study area. SST: sea surface temperature; SSS: sea surface salinity; MLD: mixed layer depth.

Station	Longitude	Latitude	Date	Time	Bottom depth (m)	SST (℃)	SSS (psu)	MLD (m)
D1	126.01	20.16	22-Dec-2015	11:21	6158	27.67	34.58	107
D3	127.70	18.62	20-Dec-2015	08:01	5023	27.56	33.60	91
D4	128.57	17.88	19-Dec-2015	20:46	5492	27.90	34.21	87
D5	129.48	17.09	19-Dec-2015	10:52	5241	27.92	34.54	86
D7	131.13	15.59	16-Dec-2015	11:00	5231	28.26	34.45	68
D8	132.14	14.86	15-Dec-2015	15:09	5609	28.06	34.22	51
D9	132.83	14.15	14-Dec-2015	22:18	5840	28.50	34.48	59
D11	134.69	12.52	13-Dec-2015	08:54	3826	28.85	34.41	59
D12	135.35	11.87	10-Dec-2015	10:30	4740	28.56	34.52	69

2.2 Hydrographic and nutrient measurements

Hydrographic parameters and water samples were collected using a Sea-Bird Electronics SBE 911 plus CTD system equipped with dual conductivity-temperature-depth sensors and an SBE 32 Carousel Water Sampler (Seabird Scientific, Bellevue, WA, USA). The CTD system continuously recorded vertical profiles of temperature, salinity, and pressure throughout the water column. Water samples from discrete depths were collected using 12-L Niskin bottles mounted on the rosette sampler for subsequent analyses of nutrients and other biogeochemical parameters. The mixed layer depth (MLD) was defined as the depth at which the potential temperature decreased by more than 0.8 ℃ from the surface value (Kara et al., 2000).

From the water samples collected at each depth, 250 mL subsamples were taken for nutrient analysis. Each subsample was filtered through pre-combusted and acid-washed Whatman GF/F filters (Whatman, UK). The filtrates were stored in 250 mL high-density polyethylene bottles and preserved with chloroform (final concentration: 2‰) to inhibit biological activity. The samples were then frozen at –20 ℃ and transported to the laboratory for analysis. Concentrations of nitrate (NO_3^--N), nitrite (NO_2^--N), phosphate (PO_4^{3-}-P), and silicate (SiO_3^{2-}-Si) were determined using an automatic nutrient analyzer (SEAL QuAAtro, Germany) (Ma et al., 2019). Dissolved inorganic nitrogen (DIN) was calculated as the sum of nitrate and nitrite concentrations. The detection limits for NO_3^--N, NO_2^--N, PO_4^{3-}-P, and SiO_3^{2-}-Si were 0.02, 0.01, 0.01, and 0.01 μmol L^{-1}, respectively.

https://doi.org/10.5194/egusphere-2026-597
Preprint. Discussion started: 23 February 2026
© Author(s) 2026. CC BY 4.0 License.

2.3 Phytoplankton pigments and primary production

To assess phytoplankton community structure, pigment analysis was conducted on seawater samples collected from each depth. A 5 L subsample was filtered through 47-mm Whatman GF/F filters under low vacuum pressure (<0.04 Mpa). Filters were immediately flash-frozen in liquid nitrogen onboard and subsequently stored at –80 ℃ until laboratory analysis. In the laboratory, filters were freeze-dried for 48 h, cut into small pieces, and extracted in the dark with 1.4 mL of 95% methanol containing 0.1 mL of 8′-apo-β-carotenal (internal standard, Sigma Chemicals, Merck KgaA, Darmstadt, Germany) under cold conditions (–20 ℃). Samples were then sonicated for 5 min at low temperature and filtered through 25-mm MFS polypropylene membrane filters (0.20 μm) to remove cellular debris. A 0.5 mL aliquot of the pigment extract was mixed with 0.1 mL of distilled water prior to analysis (Dai et al., 2022). Pigments were separated and quantified using high-performance liquid chromatography (HPLC) following the protocols of Zapata et al. (2000), using a Waters ACQUITY UPLC M-Class system equipped with a Waters Symmetry C8 column (4.6 mm × 150 mm, 3.5 μm). The mobile phases consisted of (A) methanol: acetonitrile:0.25 M aqueous pyridine solution (pH 5.0) in a 50:25:25 (v/v/v) ratio, and (B) methanol: acetonitrile: acetone in a 20:60:20 (v/v/v) ratio. The flow rate was set at 1.0 mL min^{-1}, and the column temperature was maintained at 27 ℃. Pigments were identified by comparing their retention times and absorption spectra using an online diode array detector (DAD), and quantified at 440 nm based on the internal standard method. The CHEMTAX program was then applied to estimate the relative contributions of major phytoplankton groups to total chlorophyll *a* (Chl *a*) concentrations (ng Chl *a* L^{-1}), using a pigment: Chl *a* ratio matrix adapted from Mackey et al. (1998).

Primary production (PP) was determined at stations D1, D3, D7, and D12 using the ^{14}C uptake method (Parsons et al., 1984), representing the WE, BR, CE, and KPR regions, respectively. At each station, seawater samples were collected from six depths corresponding to 100%, 50%, 30%, 10%, 5%, and 1% of surface photosynthetically active radiation (PAR), as determined from *in situ* PAR profiles measured using a quantum sensor attached to the CTD rosette system. For each light level, duplicate 250 mL seawater samples were transferred into acid-washed polycarbonate bottles and inoculated with approximately 10 μCi of $NaH^{14}CO_3$. The incubation was conducted in a deck-mounted acrylic incubation tank, which was continuously flushed with flowing surface seawater pumped from the ship to maintain ambient *in situ* temperatures. Light levels were simulated using layers of neutral-density

https://doi.org/10.5194/egusphere-2026-597
Preprint. Discussion started: 23 February 2026
© Author(s) 2026. CC BY 4.0 License.

screening mesh to achieve the desired light attenuation corresponding to each sampling depth. Incubations were performed around local noon and lasted for approximately 6 hours under natural sunlight. Following incubation, samples were gently filtered onto pre-combusted Whatman GF/F filters (25 mm) under low vacuum pressure (<0.02 MPa). Filters were exposed to concentrated HCl fumes for 12 hours to remove residual inorganic ^{14}C, then stored in scintillation vials with cocktail solution and counted using a liquid scintillation counter (Packard Tri-Carb 2200) (Gong et al., 2003). The depth-integrated daily primary production (mg C m^{-2} d^{-1}) was calculated via trapezoidal integration from the surface down to the base of the euphotic zone (defined as the 1% PAR depth).

2.4 Particle size distribution and POC flux estimation

Particle size and abundance were measured using a high-resolution Underwater Vision Profiler (UVP5-HD), mounted downward-facing on the CTD-Niskin rosette. Vertical profiles were acquired during descent at a speed of 1 m s^{-1}. The UVP captured digital images of particles illuminated within a well-defined sampling volume of 10.53 L. Particle size was determined based on the number of pixels per object in the images. Calibration of size and volume was conducted in a seawater tank using a range of natural particles to convert pixel dimensions to metric units (Picheral et al., 2010). Images were recorded at a frequency of 12 frames per second and analyzed using custom-developed image processing software. The equivalent spherical diameter (ESD) of each particle was calculated by assuming circular projected shapes. Individual particle volumes were then estimated assuming spherical geometry, and particle volume concentration (PVC; mm^3 L^{-1}) was obtained by summing all particle volumes within each depth bin and normalizing by the corresponding sampled water column. To ensure comparability with previous UVP-based studies, we restricted particle size for flux calculations to the overlapping and well-calibrated range of 100 μm to 1.5 mm (Guidi et al., 2007, 2008a; Stemmann et al., 2008; Ramondenc et al., 2016), thereby excluding particles below the resolution threshold and avoiding large-object edge effects (Fender et al., 2019). For size-structured data visualization, particles were further classified into small (ESD < 0.5 mm) and large (ESD ≥ 0.50 mm) categories following Kiko et al. (2022) and Accardo et al. (2025), which provides a useful framework for evaluating size-dependent particle dynamics such as aggregation, disaggregation, and vertical transfer.

Zooplankton data were extracted from images acquired by the UVP5-HD. Image vignettes of

https://doi.org/10.5194/egusphere-2026-597
Preprint. Discussion started: 23 February 2026
© Author(s) 2026. CC BY 4.0 License.

zooplankton were extracted from the UVP dataset and uploaded to the EcoTaxa platform (https://ecotaxa.obs-vlfr.fr, last access: 12 August 2025) for classification. An automated classification based on a random forest algorithm was applied to assign objects to broad categories, including zooplankton and non-living particles (Picheral et al., 2010). All classified images were subsequently visually inspected and manually corrected by trained analysts to ensure classification accuracy. Zooplankton abundance was calculated as the number of validated individuals in each depth bin normalized by the corresponding imaged water volume and expressed as individuals per liter (ind L^{-1}).

The POC export flux was estimated from particle size spectra using the method developed by Guidi et al. (2008a, b). The particle size distribution (PSD) typically follows a power-law decrease across the micrometer to millimeter size range (Guidi et al., 2009). Based on UVP imagery, the PSD is expressed as:

$$n(d) = \alpha d^{\beta} \quad (1)$$

where d represents particles diameter, $n(d)$ is the particle number spectrum, and β represents the slope of the log-transformed size distribution. The particle size-based carbon flux model assumes that total carbon flux (F) results from the integrated contribution of all particle sizes between a minimum (d_{min}) and maximum (d_{max}) diameter:

$$F = \int_{d_{min}}^{d_{max}} n(d) \cdot m(d) \cdot w(d) \mathrm{d}d \quad (2)$$

Here, $m(d)$ is the particle carbon mass, and $w(d)$ is the sinking velocity, estimated using Stokes' Law. Both parameters are expressed as power-law functions of particle diameter, based on empirical relationships established from joint analyses of UVP-derived PSDs and sediment trap carbon flux measurements (Guidi et al., 2008a; Jouandet et al., 2011):

$$m(d) \cdot w(d) = A d^{B} \quad (3)$$

where A and B are empirical constants. This relationship allows the discretization of the integral into logarithmic diameter bins, yielding the total carbon flux as:

$$F = \sum_{i=1}^{x} n_i \cdot A \cdot d_i^{B} \cdot \Delta d_i \quad (4)$$

In this study, we adopted values of A = 12.5 ± 3.40 and B = 3.81 ± 0.70, which represent the best-fit parameters that minimize the log-transformed residuals between sediment trap-derived and UVP-derived flux estimates across global datasets (Guidi et al., 2008a). This method has since been widely applied across a range of marine systems (Iversen et al., 2010; Ramondenc et al., 2016; Fender et al.,

https://doi.org/10.5194/egusphere-2026-597
Preprint. Discussion started: 23 February 2026
© Author(s) 2026. CC BY 4.0 License.

2019; Clements et al., 2023; Wang et al., 2024a, b), providing a robust framework for estimating size-resolved particle fluxes.

The efficiency of the biological carbon pump was assessed at stations D1, D3, D7, and D12 using the export ratio (e-ratio), calculated as the ratio of UVP-derived POC flux at 150 m to ^{14}C-based primary production integrated from the surface to the base of the euphotic zone (1% PAR depth). This approach was consistent with other studies to ensure comparability across regions with varying light penetration depths (Dunne et al., 2000; Baumann et al., 2013; Moutin et al., 2018).

2.5 Data analysis

Temperature and salinity data obtained from CTD casts, as well as particle size and abundance data derived from the UVP, were binned into 5 m vertical intervals. These binned datasets were subsequently processed to generate depth-resolved profiles of temperature, salinity, particle volume concentration, and associated POC flux estimates (Turner et al., 2017; Panaïotis et al., 2024). Statistical analyses were conducted using SPSS 25.0. Two-tailed independent-sample *t*-tests were employed to evaluate significant differences in particle and flux parameters across different depth layers and regions. Prior to applying the *t*-tests, data normality and homogeneity of variances were assessed using the Shapiro-Wilk and Levene's tests, respectively. When parametric assumptions were not met, appropriate non-parametric alternatives were used. Pearson correlation analysis was performed to examine the relationships between POC flux and environmental variables. Statistical significance was set at $p < 0.05$ unless otherwise specified. Hydrographic and particle data were visualized using Ocean Data View 4 and Origin 2022.

3 Results

3.1 Hydrographic structure and nutrient profiles

The vertical distributions of temperature and salinity along the transect were shown in Fig. 2. The SST ranged from 27.56 to 28.85 °C along the transect, generally increasing from higher to lower latitudes (Table 1). Vertically, the water column exhibited pronounced stratification, with temperatures above 27.5 °C consistently observed in the upper 50 m across the entire transect (Fig. 2a). A distinct thermocline was present starting from approximately from 50 to 100 m, with temperatures decreasing sharply with depth (Fig. 2a, c). Below 500 m, temperatures were generally below 10 °C, and dropped

https://doi.org/10.5194/egusphere-2026-597
Preprint. Discussion started: 23 February 2026
© Author(s) 2026. CC BY 4.0 License.

further to below 5 °C beneath 1000 m. The depth of the thermocline varied markedly between stations. Pronounced upward intrusions of cold water tongues were observed at stations D7, D8, and D9, as well as at D11 and D12, indicating significant thermocline shoaling in these regions (Fig. 2a). The MLD showed distinct spatial variation among the four defined regions (Table 1). In the WE region, MLD was the deepest, reaching 107 m at station D1. The BR region also exhibited relatively deep MLDs, with depths of 91 m, 81 m and 86 m at stations D3, D4 and D5, respectively. In contrast, shallower MLDs were observed in the CE region and KPR region, with 68 m, 51m, and 59 m at stations D7, D8, and D9, and 59 m and 69 m at stations D11 and D12. Overall, the MLD tended to decrease from the northwestern to southeastern stations, consistent with the weakening of surface stratification in eddy-influenced and topographically affected areas.

A subsurface high-salinity layer (>35 psu) was observed between 60 m and 200 m (Fig. 2b), which is consistent with the presence of North Pacific Subtropical Underwater (STUW) (O'Connor et al., 2002). This water mass originates from high-evaporation regions in the subtropical gyre and subducts along isopycnal towards the tropic, forming a subsurface salinity maximum in the upper thermocline. Similar with temperature, the depth of the halocline varied along the transect. At station D1, the halocline was the deepest, with the 35.0 isohaline extending to 200 m. In contrast, a noticeable shoaling of the halocline was observed at stations D7, D8, D9 and D11, and D12, where the 34.75 isohaline rose to 150 m depth.

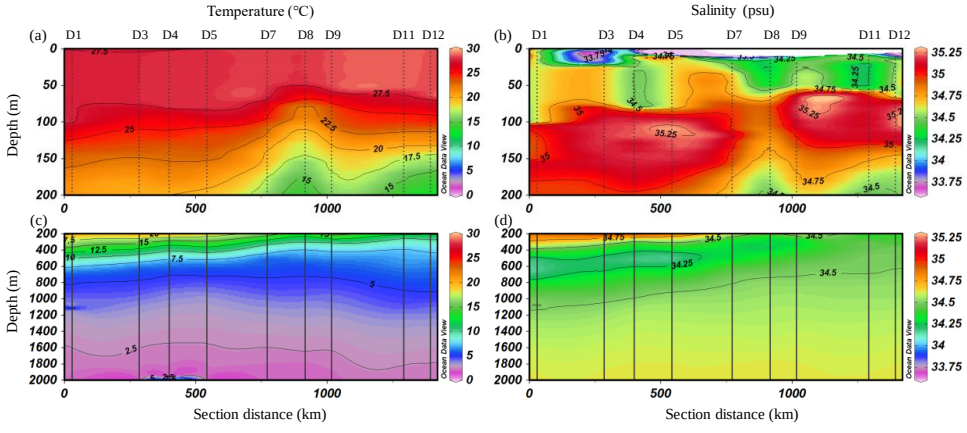

Fig. 2. Vertical distribution of temperature (°C) and salinity (psu) along the transect in the tropical Northwestern Pacific. (a) and (b) show temperature and salinity, respectively, from the surface to 200 m. (c)

https://doi.org/10.5194/egusphere-2026-597
Preprint. Discussion started: 23 February 2026
© Author(s) 2026. CC BY 4.0 License.

and (d) present the corresponding temperature and salinity distributions from 200 to 2000 m.

The vertical distributions of DIN, phosphate, and silicate concentrations along the transect are shown in Fig. 3. In the surface layer above 50 m, all three nutrients were consistently low. Similar to the temperature and salinity distributions, the vertical profiles of nutrients also exhibited pronounced variability among stations. At stations D7, D8, and D9, a clear upward displacement of nutrient-rich water was observed, with elevated concentrations reaching depths between 50 and 100 m (Fig. 3a, c, e). Similar nutrient uplift was evident at stations D11 and D12. Although the upward extension at D11 and D12 was not as shallow as that at D8, the nutrient concentrations within the uplifted water were higher. These upwelling features suggest an enhanced nutrient supply to the upper water column in these regions. Inventories of DIN, phosphate, and silicate integrated over the upper 200 m were generally higher at stations D11–D12 and D7–D9 compared to D1–D5 (Table 2). Taking DIN as an example, integrated values at D11 and D12 reached 778.76 and 944.72 mmol m^{-2}, respectively, while values at D7, D8, and D9 were 521.61, 1084.79, and 628.05 mmol m^{-2}, all substantially higher than those observed at D1 (300.34 mmol m^{-2}), D3 (224.99 mmol m^{-2}), D4 (469.73 mmol m^{-2}), and D5 (349.22 mmol m^{-2}). A similar spatial pattern was evident for phosphate and silicate. When grouped by region, the KPR area exhibited the highest nutrient inventories within the upper 200 m, followed by the CE region (Fig. 3b, d, f). In contrast, the WE and BR regions displayed the lowest integrated nutrient stocks.

https://doi.org/10.5194/egusphere-2026-597
Preprint. Discussion started: 23 February 2026
© Author(s) 2026. CC BY 4.0 License.

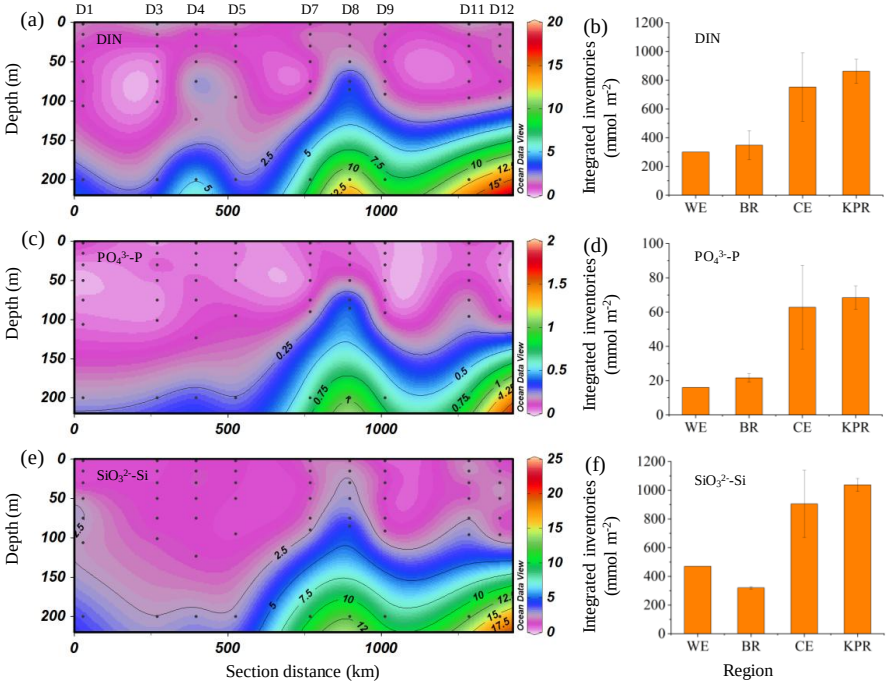

Fig. 3 Sectional distributions of nutrient concentrations (μmol L^{-1}) (a, c, e) and depth-integrated nutrient inventories (mmol m^{-2}) (b, d, f) in the upper 200 m across the four regions in the study area. a: DIN concentration (μmol L^{-1}); b: depth-integrated DIN (mmol m^{-2}); c: phosphate (μmol L^{-1}); d: depth-integrated DIN (mmol m^{-2}); e: silicate concentration (μmol L^{-1}); f: depth-integrated silicate (mmol m^{-2}). WE: warm eddy; BR: background region; CE: cold eddy; KPR: Kyushu-Palau Ridge.

Table 2. Integrated nutrient inventories (DIN, PO_4^{3-}-P, SiO_3^{2-}-Si), Chl *a*, and PVC in the upper 200 m water column; primary productivity (PP), estimated POC fluxes at 150 m, 1000 m, and 2000 m derived from UVP data; and e ratios. Missing values are indicated by —.

Station	DIN (mmol m^{-2})	PO_4^{3-}-P (mmol m^{-2})	SiO_3^{2-}-Si (mmol m^{-2})	PP (mg C $m^{-2}d^{-1}$)	Chl *a* (mg m^{-2})	PVC (L m^{-2})	Carbon $flux_{150\ m}$ (mg C $m^{-2}d^{-1}$)	Carbon $flux_{1000\ m}$ (mg C $m^{-2}d^{-1}$)	Carbon $flux_{2000\ m}$ (mg C $m^{-2}d^{-1}$)	e ratio
D1	300.34	16.03	469.58	50.02	16.58	6.66	1.63	0.70	0.53	0.03
D3	224.99	18.24	324.29	35.43	15.51	5.74	1.78	1.62	0.37	0.05
D4	469.73	23.42	326.82	—	—	6.27	1.94	0.66	0.43	—
D5	349.22	23.24	307.91	—	20.41	7.23	1.96	0.55	0.59	—
D7	542.61	49.07	810.62	68.10	20.84	7.10	2.37	1.04	1.22	0.03
D8	1084.79	97.09	1228.14	—	18.84	9.39	2.49	2.90	1.10	—
D9	628.05	42.27	678.80	—	—	13.24	2.67	1.11	1.00	—
D11	778.76	61.68	991.21	—	23.08	9.29	3.94	5.42	1.13	—

https://doi.org/10.5194/egusphere-2026-597
Preprint. Discussion started: 23 February 2026
© Author(s) 2026. CC BY 4.0 License.

D12	944.72	75.12	1083.04	142.05	21.11	24.88	13.83	5.62	5.04	0.10

343

344 **3.2 Primary productivity and phytoplankton distribution pattern**

345 PP revealed clear spatial variability along the transect (Supplementary Fig. S1a). The highest PP
346 rate was recorded at station D12 (142.05 mg C m^{-2} d^{-1}), followed by station D7 (68.10 mg C m^{-2} d^{-1}). In
347 contrast, relatively low PP rates were observed at stations D1 (50.02 mg C m^{-2} d^{-1}) and D3 (35.43 mg C
348 m^{-2} d^{-1}). Vertical distributions of total Chl *a* and group-specific Chl *a* concentrations are shown in Fig.
349 4. Overall, surface Chl *a* concentrations across the transect were low (Fig. 4a). Elevated Chl *a*
350 concentrations were detected between 50 and 100 m, indicating the presence of a pronounced deep
351 chlorophyll maximum (DCM). The highest total Chl *a* concentration (170 ng L^{-1}) was found at 75 m at
352 station D11, followed by peaks of 141 and 172 ng L^{-1} at 75 m and 90 m at station D7, respectively.
353 Among phytoplankton groups, Prochlorophytes were dominant throughout the study area, with a
354 maximum Chl *a* concentration of 85 ng L^{-1} at 75 m at station D11 (Fig. 4b). Haptophytes-6 also
355 showed significant presence, with a peak concentration of 59 ng L^{-1} at 90 m at station D7 (Fig. 4c). Chl
356 *a* associated with cyanobacteria peaked around 75 m at stations D11 and D12, with secondary maxima
357 between 50–75 m at D7 and D8 (Fig. 4d). Diatom-related Chl *a* was consistently low across all stations
358 (Fig. 4e), while Chl *a* attributed to other phytoplankton groups showed peaks around 96 m at D11 and
359 D12 (Fig. 4f). In terms of regional patterns, the KPR region exhibited the highest water column-
360 integrated Chl *a* concentration (22.1 mg m^{-2}), followed by the CE region (19.84 mg m^{-2}). The BR and
361 WE regions had the lowest values, at 17.96 mg m^{-2} and 16.59 mg m^{-2}, respectively (Supplementary Fig.
362 S1b).

https://doi.org/10.5194/egusphere-2026-597
Preprint. Discussion started: 23 February 2026
© Author(s) 2026. CC BY 4.0 License.

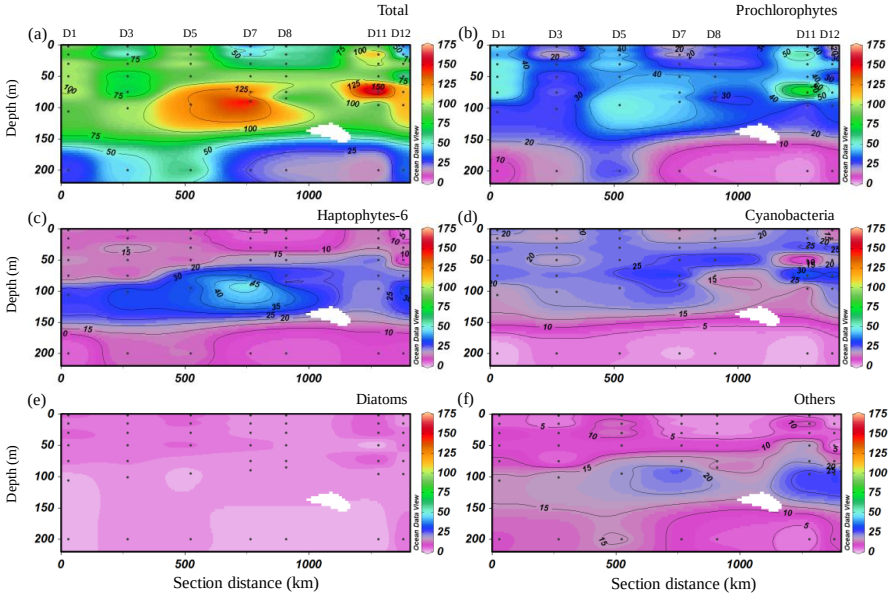

Fig. 4. Distributions of Chl *a* concentrations contributed by different taxonomic groups (ng Chl *a*·L^{-1}) in the upper 200 m of the section. a: Total; b: Prochlorophytes; c: Cyanobacteria; d: Haptophytes-6; e: Diatoms; f: Others.

https://doi.org/10.5194/egusphere-2026-597
Preprint. Discussion started: 23 February 2026
© Author(s) 2026. CC BY 4.0 License.

3.3 Spatial patterns of particle volume concentration (PVC) and their size characteristics

The vertical and horizontal distributions of PVC along the transect exhibited pronounced spatial variability (Fig. 5). In the upper 200 m, PVC ranged from nearly 0 to 0.34 $mm^3\ L^{-1}$. The highest concentrations were observed at stations D11 and D12, particularly above 100 m, with notably elevated values in the upper 50 m at station D12 (Fig. 5a). Additional PVC maxima were observed in the upper layers at D8 and D9, especially within the 10–15 m and near 100 m layers at D9. In contrast, PVC values at stations D1, D3, and D4 remained consistently low. Depth-integrated PVC (0–200 m) revealed clear regional contrasts (Table 2). The highest inventory was recorded at station D12 (24.88 L m^{-2}), followed by D9 (13.24 L m^{-2}). In contrast, stations D1, D3, and D4 showed the lowest inventories. The remaining stations displayed intermediate values, generally between 7 and 10 L m^{-2}. When grouped by subregion, the KPR region exhibited the highest mean PVC inventory within the upper 200 m, followed by the CE region. The WE and EP regions displayed the lowest values (Fig. 5b). These results clearly indicate that particle concentrations were substantially elevated in the KPR region compared to the other regions.

Below 200 m, PVC values were generally low across the transect, not exceeding 0.07 $mm^3\ L^{-1}$ (Fig. 5c, e). However, localized enhancements were evident at stations D11 and D12, where PVC reached approximately 0.05 $mm^3\ L^{-1}$. Notably, at station D12, elevated PVC extended from the surface down to nearly 1800–2000 m, forming a vertically coherent high-PVC structure. A similar but more limited enhancement was observed at station D11, primarily between 500 and 1000 m. In contrast, PVC values at most other stations remained uniformly low throughout the mesopelagic and bathypelagic layers, without distinct subsurface features.

Significant positive correlations were observed between water column integrated PVC values across successive depth ranges. Specifically, PVC integrated over 200–1000 m was significantly correlated with that in the 0–200 m layer (Fig. 6a), and PVC at 1000–2000 m was significantly correlated with that at 200–1000 m (Fig. 6b), indicating a strong vertical coupling between particle stocks in the upper and deeper layers of the water column.

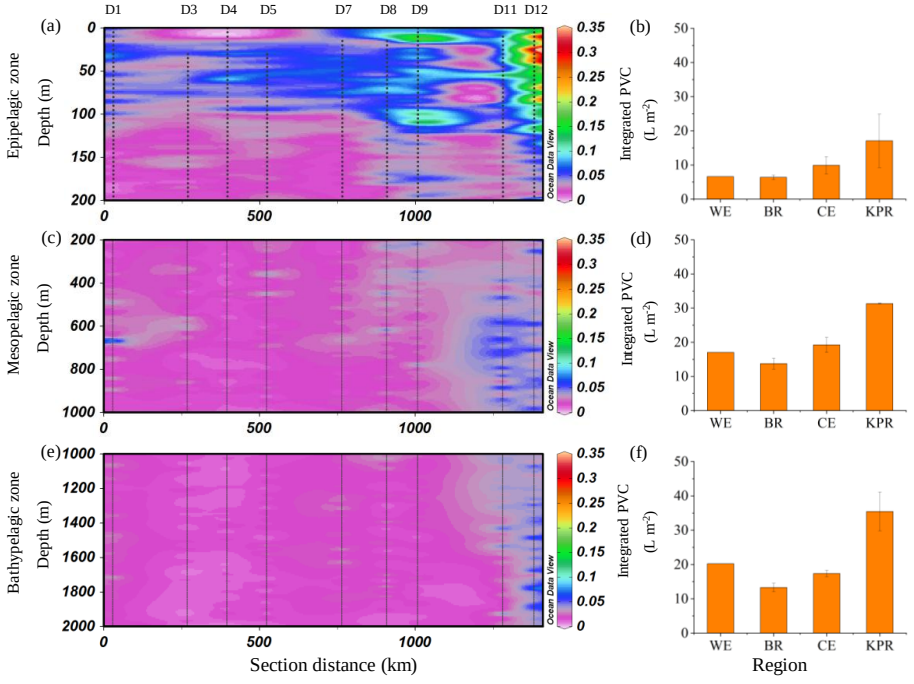

https://doi.org/10.5194/egusphere-2026-597
Preprint. Discussion started: 23 February 2026
© Author(s) 2026. CC BY 4.0 License.

Fig. 5 Sectional distributions of PVC (mm L^{-1}) and corresponding water-column inventories (L m^{-2}) in different depth layers along the transect. a, b: 0–200 m (euphotic zone); (c, d): 200–1000 m (mesopelagic zone); and (e, f) 1000–2000 m (bathypelagic zone). a, c, and e show the vertical PVC distributions along the transect, while b, d, and f present the depth-integrated PVC for the four subregions (WE, BR, CE, and KPR).

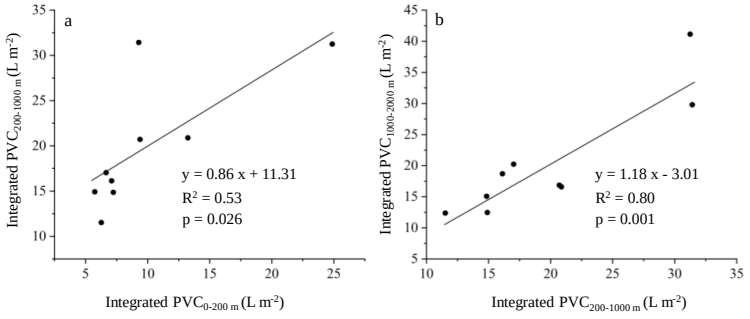

Fig. 6 Scatter plots of water column-integrated PVC at different depth ranges: (a) 0–200 m vs. 200–1000 m, and (b) 200–1000 m vs. 1000–2000 m. A significance level of $p < 0.05$ was used to determine statistical significance.

The particle size composition of PVC along the transect showed distinct spatial variability (Supplementary Fig. S2). Large particles (ESD ≥ 500 µm) were predominantly concentrated within the upper 200 m at most stations, where they accounted for a relatively high fraction of total PVC, reaching up to 50%. Below 200 m, their contribution decreased markedly and generally remained below 30%. A notable exception was observed at station D12, where large particles consistently comprised a high proportion of the total PVC throughout the water column, extending down to nearly 2000 m. At 2000 m, large particles accounted for 48% of the total PVC at D12, significantly higher than at other stations, where values were typically below 20% (*t*-test, $p < 0.05$). A pronounced maximum of zooplankton abundance (0.4 ind L^{-1}) was also detected in the upper 150 m at station D12 (Supplementary Fig. S3). Additional minor peaks were observed in the euphotic layers at stations D9 and D5, while abundances at the remaining stations remained relatively low.

3.4 POC flux and e-ratio

The vertical distribution of POC flux along the transect is presented in Fig. 7. It is evident that station D12 represents a hotspot of POC flux along the transect. Within the upper 200 m at this station, fluxes were markedly elevated, with values of 62 mg C m^{-2} d^{-1} at 25 m and 47 mg C m^{-2} d^{-1} at 40 m (Fig. 7a). Elevated fluxes at D12 extended through the mesopelagic and bathypelagic layers, where the water column maintained consistently higher values relative to other stations (Fig. 7c, e). At 2000 m, the flux reached 5.04 mg C m^{-2} d^{-1}, significantly higher than the fluxes at other stations (<1.3 mg C m^{-2} d^{-1}; *t*-test, $p < 0.05$). In addition to station D12, elevated POC fluxes were also observed at station D9 in the upper 100 m, although the magnitudes were lower than those at D12. Fluxes at D9 reached 28 mg C m^{-2} d^{-1} at 15 m and 22 mg C m^{-2} d^{-1} at 100 m (Fig. 7a). Unlike D12, the elevated flux at D9 was largely restricted to the upper 200 m, and fluxes decreased sharply downwards (Fig. 7c, e). At the remaining stations, POC fluxes were relatively low and generally did not exceed 15 mg C m^{-2} d^{-1}. From a regional perspective, the KPR region exhibited the highest average POC fluxes at all three depths (200 m, 1000 m, and 2000 m) (Fig. 7b, d, f). At 200 m, mean POC fluxes in the KPR region reached 9.04 ± 6.74 mg C m^{-2} d^{-1}, corresponding to 5.7 times and 18 times those in the CE and WE regions, respectively. At 2000 m, KPR POC fluxes remained elevated (3.09 ± 1.96 mg C m^{-2} d^{-1}), exceeding those in the CE and WE regions by factors of 2.78 and 2.73, respectively. Among the stations, the highest e-ratio was observed at D12 (10%), which was

https://doi.org/10.5194/egusphere-2026-597
Preprint. Discussion started: 23 February 2026
© Author(s) 2026. CC BY 4.0 License.

significantly higher than those at D1 (3%), D3 (5%), and D7 (3%).

Correlation analysis revealed that euphotic zone POC flux was significantly positively correlated with PVC, zooplankton abundance, and the proportion of large particles, and showed a weak positive correlation with Chl *a* concentration ($p = 0.08$) (Fig. 8). In contrast, it was significantly negatively correlated with depth and the proportion of small particles within PVC. No significant correlations were observed with the other factors.

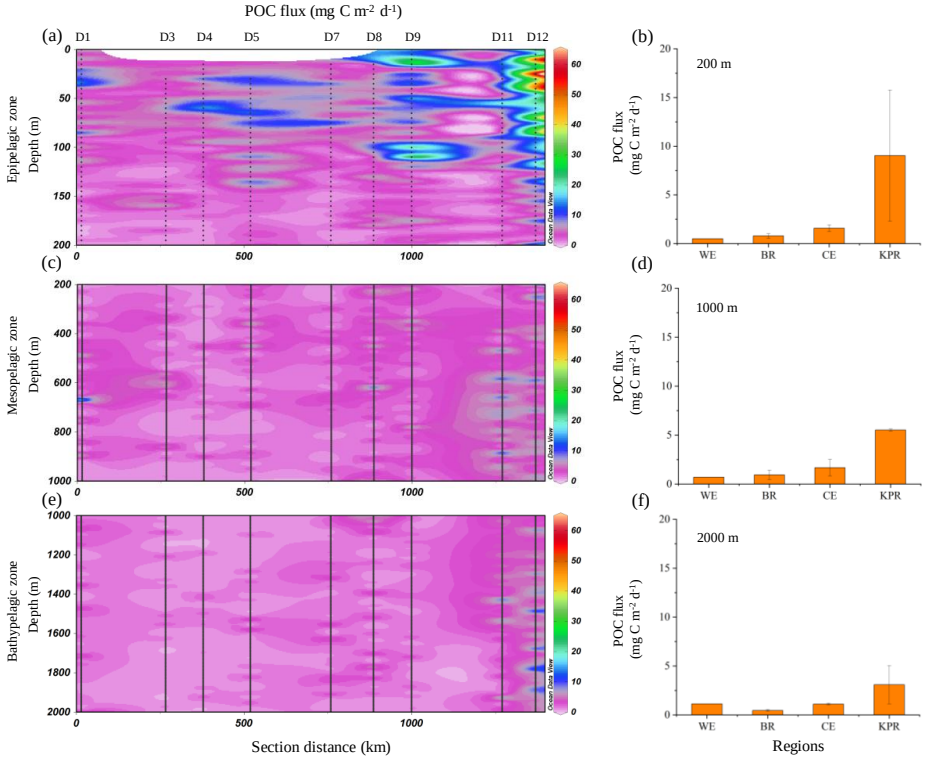

Fig. 7 Sectional distributions of POC flux (mg C m^{-2} d^{-1}) in three depth layers along the transect: (a) 0–200 m (euphotic zone), (c) 200–1000 m (mesopelagic zone), and (e) 1000–2000 m (bathypelagic zone). Panels b, d, and f compare POC fluxes at 200, 1000, and 2000 m, respectively, among the four subregions (WE, BR, CE, and KPR).

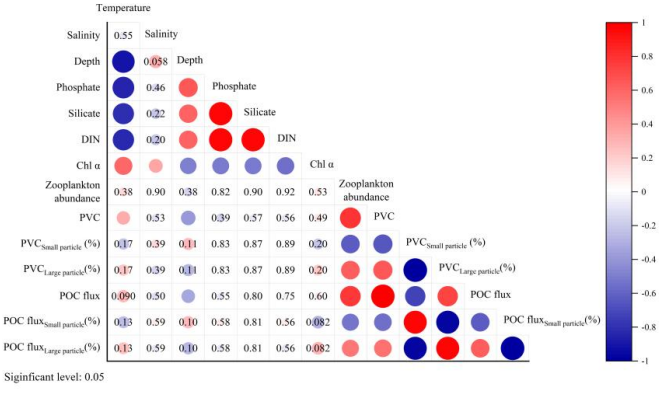

Fig. 8 Heatmap showing Pearson correlation coefficients (*r*) between POC flux and environmental as well as biological

https://doi.org/10.5194/egusphere-2026-597
Preprint. Discussion started: 23 February 2026
© Author(s) 2026. CC BY 4.0 License.

factors in the upper 200 m. Filled circles denote significant correlations ($p < 0.05$), with color intensity proportional to r, while non-significant correlations ($p \geq 0.05$) are represented solely by numeric values.

4 Discussion

4.1 Physical controls on nutrient distributions in the study area

In this study, the hydrographic structure along the transect was not spatially uniform but exhibited pronounced variability. A warm eddy was identified at station D1, while a cold eddy was observed around stations D7–D9 (Fig. 1c). In addition, evidence of thermocline uplift was detected at stations D11 and D12 (Fig. 2a, c). These two stations are located in the southern segment of the Kyushu-Palau Ridge (KPR) (Fig. 1b), where the seafloor depth is about 1000–2000 m shallower than at the other stations (Table 1). Previous studies have demonstrated that the KPR can induce upwelling through topographic effects. Xiao et al. (2023) identified a diapycnal upwelling over the KPR, with enhanced vertical mixing and upward isopycnal displacement occurring primarily beneath the thermocline and extending down to 1000 m. Song et al. (2024) also reported persistently enhanced turbulent mixing over the KPR, with diapycnal diffusivity beneath the thermocline elevated by 1–2 orders of magnitude, supporting the presence of topography-induced upwelling. Therefore, the transect in this study exhibited pronounced variations in physical conditions, ranging from a warm eddy region in the northwest, to a background zone, a cold eddy region, and finally a ridge-induced upwelling area in the southeast (Fig. 1c). This transect thus encompassed four distinct physical regimes, providing an excellent opportunity to investigate how different physical processes shape the biogeochemical variability and carbon cycling in the tropical Northwestern Pacific.

Nutrient concentrations in the upper 100 m of the water column were very low (Fig. 3a, c, and e), consistent with previous report on nutrients level in this region (Ma et al., 2021). However, distinct nutrient upwelling was observed below 100 m at stations D8 and D12 and in their surrounding areas (Fig. 3a, c, and e). At station D8, the upward intrusion extended to depths of 50–100 m, while at station D12, upwelling reaching approximately 100 m, with substantially higher nutrient concentrations. No such upwelling signal was detected at other stations. This suggests that both the upwelling over the KPR and the cold eddy play important roles in supplying nutrients to the euphotic zone. While the vertical nutrient transport associated with cold eddies has been documented in previous studies (Guidi et al., 2012; Shih et al., 2015; Moutin et al., 2018), this study highlights the significant contribution of the KPR-induced upwelling for the first time. Depth-integrated nutrient inventories in the upper 200 m showed that DIN, phosphate, and silicate were all highest in the KPR region (Fig. 3b, d, f), indicate that the upwelling induced by the KPR supplied more nutrients to the euphotic zone than the other regions, including the cold eddy. As a prominent ridge system, the upwelling induced by KPR often originates from deeper layers (Xiao et al., 2023). This is supported by the temperature section, where pronounced thermocline uplift was observed at 400–600 m at stations D11 and D12 (Fig. 2c). The upwelled water likely originates from the Lower Circumpolar Deep Water (LCDW), which is a cold, nutrient-rich water mass that enters the Philippine Sea via the Yap-Mariana Junction and is uplifted along isopycnals as it interacts with KPR topography (Xiao et al., 2023). Although the CE region is also characterized by upwelling, the vertical transport is generally confined to shallower layers, typically within the upper thermocline (Ueno et al., 2023). Such mesoscale eddy-induced upwelling primarily redistributes nutrient-depleted surface or subsurface waters (Ding et al., 2022; Kang et al., 2022). This fundamental difference in the source depth and nutrient content of upwelled waters likely explains the markedly higher nutrient inventories observed in the KPR region compared to the CE region.

In other parts of the transect, nutrient concentrations in the upper 200 m were generally low at the warm eddy (WE) and background (BR) stations (Fig. 3a, c, e). In terms of water-column nutrient inventories, the integrated

https://doi.org/10.5194/egusphere-2026-597
Preprint. Discussion started: 23 February 2026
© Author(s) 2026. CC BY 4.0 License.

concentrations of DIN, phosphate, and silicate in these two regions were significantly lower than those in the KPR area (Fig. 3b, d, f). This pattern is associated with the strong downwelling within the warm eddy and the lack of substantial vertical transport processes in the background region. In general, both the hydrographic structure and nutrient distributions along the transect exhibited pronounced spatial variability, reflecting the influence of distinct physical processes. In the KPR region, topographic control by the ridge generated strong upwelling that brought nutrient-rich deep water into the upper layers, resulting in substantially higher nutrient inventories within the upper 200 m compared with other regions. In contrast, although the cold eddy also showed signs of upwelling, the nutrient concentrations of the uplifted waters were lower, yielding intermediate nutrient inventories. The warm eddy and background regions, lacking effective vertical transport, maintained persistently low nutrient levels throughout the water column. These contrasting physical processes represent the primary drivers of spatial differences in nutrient supply capacity across the transect.

4.2 Contrasting primary productivity and phytoplankton biomass between KPR and other regions

In this study, primary productivity ranged from 35.43 to 142.05 mg C m^{-2} d^{-1} (Table 2), which is lower than that reported for most other regions of the Pacific Ocean. For example, in the subarctic northeastern Pacific, primary productivity ranges between 200 and 600 mg C m^{-2} d^{-1} (Whitney et al., 2005). In the eastern tropical Pacific, primary production shows a pronounced spatial gradient, exceeding 1000 mg C m^{-2} d^{-1} in the equatorial upwelling zone and decreasing to less than 300 mg C m^{-2} d^{-1} in the oligotrophic subtropical gyres (Pennington et al., 2006). In the northwestern subtropical Pacific, values range from approximately 108 to 847 mg C m^{-2} d^{-1}, with an annual mean of about 303 mg C m^{-2} d^{-1} (Matsumoto et al., 2016). These comparisons indicate that the study area represents a low-productivity region within the Pacific Ocean. Although primary productivity along the transect was generally low, it exhibited pronounced station-to-station variability. The spatial variability in primary productivity observed along the transect was closely linked to differences in MLD (Table 1), which reflects the degree of vertical mixing and nutrient entrainment in the upper layer. Several studies have found that shallower MLD are often associated with enhanced surface primary production, as they promote greater light availability and facilitate the injection of nutrients into the euphotic zone (Van Ruth et al., 2010; Kumar and Narvekar, 2005). However, deeper mixed layers can dilute phytoplankton into low-light environments and limit nutrient delivery, leading to reduced productivity (Schofield et al., 2018). In the KPR region, isotherms showed a pronounced shoaling pattern in the upper 200 m with a shallower MLD (Fig. 2a), indicative of topography-induced upwelling. This shoaling facilitated the upward transport of deep, nutrient-rich waters into the euphotic zone, thereby enhancing nutrient availability for phytoplankton growth. As a result, station D12 exhibited significantly higher primary productivity (142. 05 mg C m^{-2} d^{-1}) compared to the background station D3 (35. 43 mg C m^{-2} d^{-1}), representing a nearly fourfold increase (Fig. S1a, $p < 0.05$). This indicates a substantial enhancement of surface productivity driven by ridge-induced upwelling.

The distribution of phytoplankton along the transect also exhibited pronounced spatial variability. High phytoplankton biomass was observed near station D7, influenced by the cold eddy, and around stations D11 and D12, located in the KPR region (Fig. 4a). In contrast, low biomass was detected in the northwestern region (stations D1 and D3), reflecting the oligotrophic nature of this area. The most dominant phytoplankton group in this area was *Prochlorococcus* (Fig. 4b), consistent with previous findings from surveys in adjacent regions such as the North Equatorial Current and the western Pacific warm pool (Zhang et al., 2023; An et al., 2025). *Prochlorococcus* exhibited notably higher abundances in the upper layers at stations D11 and D12, while remaining relatively low at other stations (Fig. 4b). This distribution pattern suggests that *Prochlorococcus* populations respond positively

https://doi.org/10.5194/egusphere-2026-597
Preprint. Discussion started: 23 February 2026
© Author(s) 2026. CC BY 4.0 License.

to moderate nutrient enrichment condition induced by topographic upwelling over the KPR. When compared across regions, the KPR region also exhibited the highest depth-integrated Chl *a* concentrations (Supplementary Fig. S1b). These results indicate that the spatial variability of the physical environment across the transect, through its control on nutrient availability, played a key role in shaping the distribution pattern of phytoplankton.

4.3 Enhanced carbon export and e-ratio in the ridge-associated region

In this study, the UVP-derived POC flux in the upper 200 m ranged from 0.38 to 61.82 mg C m^{-2} d^{-1}, with an average of 6.16 ± 7.63 mg C m^{-2} d^{-1}. This range is comparable to the results obtained using the ^{210}Po-^{210}Pb disequilibria method in the western North Pacific (upper 150 m: 7.2–105.6 mg C m^{-2} d^{-1}; Zhong et al., 2021) and is also consistent with sediment trap measurements at 100 m depth (12–40.8 mg C m^{-2} d^{-1}; Seo et al., 2022). However, it is lower than the values reported for the central equatorial Pacific, where fluxes at 150°W reached 146.4 mg C m^{-2} d^{-1} due to elevated surface nitrate concentrations (Dunne et al., 2000), and slightly lower than those observed in the western tropical South Pacific, where POC fluxes at 150 m averaged 13.2 mg C m^{-2} d^{-1} in the Melanesian Archipelago (Moutin et al., 2018). Overall, the POC fluxes observed in this study fall within the typical range reported for tropical oligotrophic ocean regions.

Significant correlations between water column integrated PVC across successive depth ranges (Fig. 6) suggest that particle fluxes in the mesopelagic and bathypelagic layers are largely sustained by the gravitational settling of particles originating from the upper ocean. This strong vertical coupling indicates an efficient transfer of surface derived particulate matter to depth. Along the transect, a pronounced hotspot of POC flux was observed at station D12 within the epipelagic zone (Fig. 7a). Regionally, the POC flux at 200 m depth in the KPR area was significantly higher than in the other three regions, with mean values approximately 19, 12, and 6 times greater than those in the WE, BR, and CE regions, respectively (Fig. 7b). Notably, elevated POC fluxes in the KPR region were also evident in both the mesopelagic and bathypelagic zones (Fig. 7c-f), indicating that the enhancement of POC flux above the KPR extended throughout the whole water column. The enhancement of POC flux in this region is consistent with the spatial patterns of nutrients and phytoplankton observed above. Upwelling induced by the Kyushu-Palau Ridge elevated nutrient concentrations within the euphotic zone compared to other regions (Fig. 3), consequently stimulating higher primary productivity and phytoplankton biomass (Supplementary Fig. S1). In addition, PVC in the epipelagic zone was significantly higher in the KPR region than in the other areas (Fig. 5), and this region was characterized by a markedly increased contribution of large particles (ESD ≥ 500 μm) (Supplementary Fig. S2). These results suggest that elevated nutrient availability promoted phytoplankton growth, which in turn enhanced particle production, possibly through aggregation processes, which is one of the main mechanisms contributing to the observed increase in POC flux (Fig. 8). In addition, previous studies have shown that even in oligotrophic regions where phytoplankton communities are dominated by pico- and nano-phytoplankton, phytoplankton carbon can still be efficiently exported to depth through zooplankton grazing and fecal pellet production (Richardson and Jackson, 2007). In this study, zooplankton abundance in the upper 150 m at station D12 in the KPR region was markedly higher than at other stations, reaching up to 0.32 ind L^{-1}, whereas abundances at most other stations remained below 0.15 ind L^{-1} (Supplementary Fig. S3a). The elevated zooplankton abundance in the KPR region indicates more intense grazing activity, which enhances the packaging of small phytoplankton cells into rapidly sinking fecal pellets. Although individual phytoplankton cells generally exhibit low sinking velocities, typically on the order of a few meters per day, zooplankton fecal pellets can sink at rates one to two orders of magnitude faster, reaching rates of tens to over a hundred meters per day (Turner, 2015). The sinking of zooplankton-mediated particles likely contributed to the enhanced POC flux observed above the

https://doi.org/10.5194/egusphere-2026-597
Preprint. Discussion started: 23 February 2026
© Author(s) 2026. CC BY 4.0 License.

ridge. Therefore, the biological carbon pump appears to be significantly strengthened in the KPR region, where topography-induced upwelling enhances nutrient supply and reinforces the coupling between surface primary production and deep carbon export through particle aggregation and zooplankton packaging.

In addition to POC flux, we also calculated the e-ratio, which represents the efficiency of the biological carbon pump, that is, the fraction of primary production that is exported as sinking POC from the euphotic zone (Henson et al., 2012). In this study, e-ratio values ranged from 0.03 to 0.10 (Table 2). This range is comparable to that in the western tropical South Pacific Ocean, where the mean e-ratio was approximately 0.06 in the Melanesian Archipelago and 0.02 in the South Pacific Gyre (Moutin et al., 2018). However, the values are markedly lower than those observed in several shelf regions, such as the eastern Bering Sea shelf break (0.21, Baumann et al., 2013) and the East China Sea (0.16–0.59; Hung et al., 2016), as well as in the Southern Ocean, where e-ratio values range from 0.07 to 0.97 (Fan et al., 2020). These comparisons indicate that the study area represents a typical low efficiency BCP region. Despite the overall low e-ratio, a clear spatial contrast was observed, with station D12 in the KPR region exhibiting a significantly higher e-ratio (0.10) than the other stations (e-ratio < 0.06), suggesting a locally enhanced biological pump efficiency associated with the ridge-induced upwelling. Several studies have been carried out to identify which particle size classes contribute most to the export of POC from the surface to the deep ocean. Most studies consistently indicate that large particles account for the dominant fraction of total POC flux (Stemmann et al., 2008; Riley et al., 2012). Larger particles tend to sink faster and contribute more efficiently to the downward transport of POC, whereas smaller particles tend to sink slowly and are more susceptible to remineralization and recycling in the upper ocean (Huang et al., 2022). In this study, a markedly higher proportion of large particles (ESD ≥ 500 μm) within the PVC was observed throughout the entire water column at station D12 and below 500 m at station D11, compared with other stations along the transect (Supplementary Fig. 2). At station D12, the fraction of large particles reached over 60% in the euphotic zone and remained as high as 40% even in the bathypelagic layer, whereas the proportion at other stations was generally below 20%. This region was characterized by elevated primary productivity and phytoplankton biomass (Supplementary Fig. S1), which could favor the formation of large marine aggregates through enhanced adhesion among phytoplankton cells and between cells and other suspended particles (De La Rocha and Passow, 2007). Moreover, the high food availability supported a substantially greater abundance of zooplankton here (Supplementary Fig. S3a). The presence of large zooplankton individuals likely contributed to the increased proportion of large particles, both directly through their own contribution and indirectly via the production of large fecal pellets after feeding on phytoplankton, which typically have high sinking velocities (Stamieszkin et al., 2017; Wang et al., 2023b; Xu et al., 2025). Therefore, the enhanced aggregation of phytoplankton-derived particles and the packaging of organic matter into fast-sinking fecal pellets likely acted together to increase the proportion of large particles in the KPR region, ultimately strengthening the BCP efficiency above the Ksushu-Palau Ridge.

4.4 Biogeochemical and ecological implications

The elevated carbon export and efficiency observed in the KPR region have important implications for the regional carbon cycle and ecosystem functioning. The tropical western Pacific is generally characterized as a typical oligotrophic environment, where the efficiency of the biological carbon pump is considered to be low (Zhong et al., 2021). In such regions, the majority of POC is thought to be remineralized within the upper ocean, and thus this area has traditionally been regarded as a minor contributor to the global oceanic carbon export (Wang et al., 2023a). However, this study revealed remarkably high carbon export fluxes and efficiencies in the KPR region, where the enhancement effect associated with topography-induced upwelling appeared to be even stronger

https://doi.org/10.5194/egusphere-2026-597
Preprint. Discussion started: 23 February 2026
© Author(s) 2026. CC BY 4.0 License.

than that driven by mesoscale eddies. Previous studies have generally suggested that mesoscale eddies are the primary mechanism enhancing surface primary production and POC export in the western tropical Pacific (Shih et al., 2015; Seo et al., 2022). In contrast, our results indicate that the upwelling induced by the ridge plays an even more important role in promoting vertical nutrient supply and strengthening the BCP, which was paid to little attention in previous studies. Considering that the KPR extends for approximately 2600 km and covers nearly 21% of the deep-water area of the Philippine Sea (Xiao et al., 2023), and that it represents a persistent and year-round topographic feature, the carbon export effect associated with the upwelling deserves particular attention. Beyond the study area, ridges are widely distributed throughout the global ocean, including the Sulu Ridge in the South China Sea (Jing et al., 2012), the Seychelles-Chagos Thermocline Ridge in the Indian Ocean (Vinayachandran et al., 2021), the Mid-Atlantic Ridge in the North Atlantic (Abell et al., 2013), and the East Pacific Rise in the South Pacific (Rowler et al., 2016). Upwelling associated with these ridges has been widely observed, suggesting that their role in biological carbon export is not limited to regional settings. The influence of ridge-induced upwelling should be considered in future studies and models of the global ocean carbon cycle.

Previous studies have also shown that the seafloor in the KPR region supports higher benthic biodiversity and biomass compared with surrounding areas (Lu et al., 2024). However, the source of organic matter sustaining such benthic hotspots remain unclear. The results of this study suggest that the enhanced deep POC flux associated with ridge-induced upwelling is likely a key factor supporting the benthic community. The upwelling and subsequent enhancement of carbon export driven by ridge topography may thus play an important role in shaping global patterns of benthic biodiversity, which also warrants further investigation.

5 Conclusion

In this study, we applied a multidisciplinary observational approach to investigate phytoplankton productivity and biological carbon pump processes along a meridional transect in the tropical Northwestern Pacific. Our results revealed that the KPR region exhibited elevated nutrient concentrations in the upper 200 m, attributable to topographically induced upwelling. Notably, nutrient inventories in the KPR region were even higher than those observed in the cold eddy, where upwelling is typically expected. In contrast, no significant nutrient enrichment was found in the warm eddy or background regions. Corresponding to the elevated nutrients, the euphotic zone primary production, phytoplankton biomass, and PVC were all significantly higher in the KPR region compared to the other zones. Enhanced abundances of large particles and zooplankton in this region contributing to higher POC fluxes throughout the water column. As a result, the e-ratio in the KPR region was substantially elevated relative to other regions. These findings underscore the critical role of ridge-induced upwelling in enhancing biological carbon pump, highlighting the biogeochemical significance of submarine ridge systems in oligotrophic oceans.

Data Availability Statement

Data available on request from the authors.

Author Contribution

SG: Conceptualization, Data curation, Formal analysis, Methodology, Software, Visualization, Writing-original draft preparation. MZ: Data curation, Formal analysis, Investigation, Methodology, Validation. SZ: Data curation,

https://doi.org/10.5194/egusphere-2026-597
Preprint. Discussion started: 23 February 2026
© Author(s) 2026. CC BY 4.0 License.

Investigation. WX: Data curation. JS: Data curation, Investigation. YZ: Data curation, Formal analysis. SD: Data curation, Formal analysis. JL: Investigation. CZ: Visualization. XS: Conceptualization, Funding acquisition, Project administration, Supervision, Writing-review&editing.

Competing interests

The authors declare that they have no conflict of interest.

Disclaimer

Publisher's note: Copernicus Publications remains neutral with regard to jurisdictional claims made in the text, published maps, institutional affiliations, or any other geographical representation in this paper. While Copernicus Publications makes every effort to include appropriate place names, the final responsibility lies with the authors.

Acknowledgements

We thank the crew and captain of the R/V *Kexue* for the logistic support during the cruise.

Financial support

This work was supported by the National Natural Science Foundation of China (No. 42530412, 32371619).

References

Abell, R. E., Brand, T., Dale, A. C., Tilstone, G. H., Beveridge, C.: Variability of particulate flux over the Mid-Atlantic Ridge. Deep-Sea Research II, 98, 257–268, https://doi.org/10.1016/j.dsr2.2013.10.005, 2013.

Accardo, A., Laxenaire, R., Baudena, A., Speich, S., Kiko, R., Stemmann, L.: Intense and localized export of selected marine snow types at eddy edges in the South Atlantic Ocean. Biogeosciences, 22, 1183–1201, https://doi.org/10.5194/bg-22-1183-2025, 2025.

An, L. N., Liu, X., Xu, F. P., Fan, X. Y., Wang, P. X., Yin, W. F., Huang, B. Q.: Different responses of plankton community to mesoscale eddies in the western equatorial Pacific Ocean. Deep Sea Research I, 203, 104219, https://doi.org/10.1016/j.dsr.2023.104219, 2024.

An, L. N., Huang, Y. B., Xu, C., Xu, F. P., Chen, J. X., Liu, X., Huang, B. Q.: Biogeochemical characteristics and phytoplankton community diversity of the Western North Equatorial current. Global and Planetary Change, 252, 104895, https://doi.org/10.1016/j.gloplacha.2025.104895, 2025.

Baumann, M. S., Moran, S. B., Lomas, M. W., Kelly, R. P., Bell, D. W.: Seasonal decoupling of particulate organic carbon export and net primary production in relation to sea-ice at the shelf break of the eastern Bering Sea: Implications for off-shelf carbon export. Journal of Geophysical Research, 118, 5504–5522, https://doi.org/10.1002/jgrc.20366, 2013.

Bressac, M., Laurenceau-Cornec, E. C., Kennedy, F., Santoro, A. E., Paul, N. L., Briggs, N., Carvalho, F., Boyd, P. W.: Decoding drivers of carbon flux attenuation in the oceanic biological pump. Nature, 633, 587–593, https://doi.org/10.1038/s41586-024-07850-x, 2024.

Clements, D. J., Yang, S., Weber, T., McDonnell, A. M. P., Kiko, R., Stemmann, L., Bianchi, D.: New estimate of organic carbon export from optical measurements reveals the role of particle size distribution and export horizon. Global Biogeochemical Cycles, 37, e2022GB007633, https://doi.org/10.1029/2022GB007633, 2023.

Dai, S., Zhao, Y. F., Li, X. G., Wang, Z. Y., Zhu, M. L., Liang, J. H., Liu, H. J., Sun, X. X.: Seamount effect on phytoplankton biomass and community above a deep seamount in the tropical western Pacific. Marine Pollution Bulletin, 175, 113354, https://doi.org/10.1016/j.marpolbul.2022.113354, 2022.

https://doi.org/10.5194/egusphere-2026-597
Preprint. Discussion started: 23 February 2026
© Author(s) 2026. CC BY 4.0 License.

Dang, X. Y., Chen, X. Y., Bai, Y., He, X. Q., Arthur Chen, C. T., Li, T., Pan, D. L., Zhang, Z. K.: Impacts of ENSO events on phytoplankton over the Sulu Ridge. Marine Environmental Research, 157, 104934, https://doi.org/10.1016/j.marenvres.2020.104934, 2020.

De La Rocha, C. L., Passow, U.: Factors influencing the sinking of POC and the efficiency of the biological carbon pump. Deep-Sea Research II, 54, 639–658, https://doi.org/10.1016/j.dsr2.2007.01.004, 2007.

DeVries, T., Primeau, F., Deutsch, C.: The sequestration efficiency of the biological pump. Geophysical Research Letters, 39, L13601, https://doi.org/10.1029/2012GL051963, 2012.

Ding, Y. N., Yu, F., Ren, Q., Nan, F., Wang, R., Liu, Y. S., Tang, Y.: The physical-biogeochemical responses to a subsurface anticyclonic eddy in the Northwest Pacific. Frontiers in Marine Science, 8, 766544, https://doi.org/10.3389/fmars.2021.766544, 2022.

Dunlop, K. M., van Oevelen, D., Ruhl, H. A., Huffard, C. L., Kuhnz, L. A., Smith, Jr. K. L.: Carbon cycling in the deep eastern North Pacific benthic food web: Investigating the effect of organic carbon input. Limnology and Oceanography, 61, 1956–1968, https://doi.org/10.1002/lno.10345, 2016.

Dunne, J. P., Murray, J. W., Rodier, M., Hansell, D. A.: Export flux in the western and central equatorial Pacific: zonal and temporal variability. Deep-Sea Research I, 47, 901–936, https://doi.org/10.1016/S0967-0637(99)00089-8, 2000.

Fan, G. J., Han, Z. B., Ma, W. T., Chen, S. L., Chai, F., Mazloff, M. R., Pan, J. M., Zhang, H. S.: Southern Ocean carbon export efficiency in relation to temperature and primary productivity. Scientific Reports, 10, 13494, https://doi.org/10.1038/s41598-020-70417-z, 2020.

Fender, C. K., Kelly, T. B., Guidi, L., Ohman, M. D., Smith M, C., Stukel, M. R.: Investigating particle size-flux relationships and the biological pump across a range of plankton ecosystem states from coastal to oligotrophic. Front. Mar. Sci., 6, 603, https://doi.org/10.3389/fmars.2019.00603, 2019.

Gong, G. C., Wen, Y. H., Wang, B. W., Liu, G. J.: Seasonal variation of chlorophyll *a* concentration, primary production and environmental conditions in the subtropical East China Sea. Deep Sea Res. II, 50, 1219–1236, https://doi.org/10.1016/S0967-0645(03)00019-5, 2003.

Guidi, L., Stemmann, L., Legendre, L., Picheral, M., Prieur, L., Gorsky, G: Vertical distribution of aggregates (>100 µm) and mesoscale activity in the Northeastern Atlantic: effects on the deep vertical export of surface carbon. Limnol. Oceanogr., 52, 7–18, https://doi.org/10.4319/lo.2007.52.1.0007, 2007.

Guidi, L., Jackson, G. A., Stemmann, L., Miquel, J. C., Picheral, M., Gorsky, G: Relationship between particle size distribution and flux in the mesopelagic zone. Deep-Sea Res. PT I, 55, 1364–1374, https://doi.org/10.1016/j.dsr.2008.05.014, 2008a.

Guidi, L., Gorsky, G., Claustre, H., Miquel, J. C., Picheral, M., Stemmann, L.: Distribution and fluxes of aggregates >100 µm in the upper kilometer of the South-Eastern Pacific. Biogeosciences, 5, 1361–1372, https://doi.org/10.5194/bg-5-1361-2008, 2008b.

Guidi, L., Stemmann, L., Jackson, G. A., Ibanez, F., Claustre, H., Legendre, L., Picheral, M., Gorsky, G.: Effects of phytoplankton community on production, size, and export of large aggregates: a world-ocean analysis. Limnol. Oceanogr., 54(6), 1951–1963, https://doi.org/10.4319/lo.2009.54.6.1951, 2009.

Henson, S. A., Sanders, R., Madsen, E.: Global patterns in efficiency of particulate organic carbon export and transfer to the deep ocean. Global Biogeochemical Cycles, 26(1), https://doi.org/10.1029/2011GB004099, 2012.

Henson, S. A., Le Moigne, F. A., Giering, S. L.: Drivers of carbon export efficiency in the global ocean. Global Biogeochemical Cycles, 33(9), 891–903, https://doi.org/10.1029/2018GB006158, 2019.

https://doi.org/10.5194/egusphere-2026-597
Preprint. Discussion started: 23 February 2026
© Author(s) 2026. CC BY 4.0 License.

Huang, Y. B., Fassbender, A. J., Long, J. S., Johannessen, S., Bif, M. B.: Partitioning the export of distinct biogenic carbon pools in the Northeast Pacific Ocean using a biogeochemical profiling float. Global Biogeochemical Cycles, 36(2), e2021GB007178, https://doi.org/10.1029/2021GB007178, 2022.

Hung, C. C., Chen, Y. F., Hsu, S. C., Wang, K., Chen, J. F., Burdige, D. J.: Using rare earth elements to constrain particulate organic carbon flux in the East China Sea. Scientific Reports, 6, 33880, https://doi.org/10.1038/srep33880, 2016.

Iversen, M. H., Nowald, N., Ploug, H., Jackson, G. A., Fischer, G.: High resolution profiles of vertical particulate organic matter export off Cape Blanc, Mauritania: degradation processes and ballasting effects. Deep-Sea Res. PT I, 57(6), 771–784, https://doi.org/10.1016/j.dsr.2010.03.007, 2010.

Iversen, M. H.: Carbon export in the ocean: a biologist's perspective. Annual Review of Marine Science, 15, 357–381, https://doi.org/10.1146/annurev-marine-032122-035153, 2023.

Jing, Z. Y., Qi, Y. Q., Du, Y.: Persistent upwelling and front over the Sulu Ridge and their variations. Journal of Geophysical Research, 117, C11011, https://doi.org/10.1029/2012JC008355, 2012.

Jouandet, M. P., Trull, T. W., Guidi, L., Picheral, M., Ebersbach, F., Stemmann, L., Blain, S.: Optical imaging of mesopelagic particles indicates deep carbon flux beneath a natural iron-fertilized bloom in the Southern Ocean. Limnol. Oceanogr., 56(3), 1130–1140, https://doi.org/10.4319/lo.2011.56.3.1130, 2011.

Kang, J. H., Wang, Y., Huang, S. H., Pei, L. L., Luo, Z. H.: Impacts of mesoscale eddies on biogeochemical variables in the Northwest Pacific. Journal of Marine Science and Engineering, 10, 1451, https://doi.org/10.3390/jmse10101451, 2022.

Kara, A. B., Rochford, P. A., Hurlburt, H. E.: An optimal definition for ocean mixed layer depth. Journal of Geophysical Research, 105, 16803–16821, https://doi.org/10.1029/2000JC900072, 2000.

Kiko, R., Picheral, M., Antoine, D., Babin, M., Berline, L., Biard, T., Boss, E., Brandt, P., Carlotti, F., Christiansen, S., Coppola, L., de la Cruz, L., Diamond-Riquier, E., de Madron, X. D., Elineau, A., Gorsky, G., Guidi, L., Hauss, H., Irisson, J. O., Karp-Boss, L., Karstensen, J., Kim, D., Lekanoff, R. M., Lombard, F., Lopes, R. M., Marec, C., Mcdonnell, A. M. P., Niemeyer, D., Noyon, M., O'Daly, S. H., Ohman, M. D., Pretty, J. L., Rogge, A., Searson, S., Shibata, M., Tanaka, Y., Tanhua, T., Taucher, J., Trudnowska, E., Turner, J. S., Waite, A., Stemmann, L.: A global marine particle size distribution dataset obtained with the Underwater Vision Profiler 5. Earth Syst. Sci. Data, 14, 4315–4337, https://doi.org/10.5194/essd-14-4315-2022, 2022.

Kumar, S. P., Narvekar, J.: Seasonal variability of the mixed layer in the central Arabian Sea and its implication on nutrients and primary productivity. Deep Sea Research II, 52(14–15), 1848–1861, https://doi.org/10.1016/j.dsr2.2005.06.002, 2005.

Kwon, E. Y., Primeau, F., Sarmiento, J. L.: The impact of remineralization depth on the air-sea carbon balance. Nat. Geoscience, 2, 630–635, https://doi.org/10.1038/ngeo612, 2009.

Louchard, D., Gruber, N., Münnich, M.: The impact of the Amazon on the biological pump and the air-sea CO_2 balance of the western Tropical Atlantic. Global Biogeochemical Cycles, 35(6), e2020GB006818, https://doi.org/10.1029/2020GB006818, 2021.

Lu, X., Shen, C. C., Yang, C. H., Xu, W. K., Yang, J., Wang, C. S., Sun, D.: Megabenthic diversity patterns on a seamount in the Philippine Sea: Implications for conservation planning on the Kyushu-Palau Ridge. Ecology and Evolution, 14, e70427, https://doi.org/10.1002/ece3.70427, 2024.

Ma J, Song J M, Li X G, Yuan H M, Li N, Duan L Q, Wang Q D. 2019. Environmental characteristics in three

https://doi.org/10.5194/egusphere-2026-597
Preprint. Discussion started: 23 February 2026
© Author(s) 2026. CC BY 4.0 License.

seamount areas of the tropical Western Pacific Ocean: focusing on nutrients. Marine Pollution Bulletin, 143: 163-174.

Ma J, Song J M, Li X G, Wang Q D, Sun X X, Zhang W C, Zhong G R. 2021. Seawater stratification vs. plankton for oligotrophic mechanism: A case study of M4 seamount area in the Western Pacific Ocean. Marine Environmental Research, 169: 105400.

Macdonald K C. 2001. Mid-ocean ridge tectonics, volcanism and geomorphology. Encyclopedia of Ocean Sciences Elsevier 1798–1813.

Mackey D J, Higgins H W, Mackey M D, et al. 1998. Algal class abundances in the western equatorial Pacific: estimation from HPLC measurements of chloroplast pigments using CHEMTAX. Deep-Sea Res. I, 45(9):.

Matsumoto K, Abe O, Fujiki T, Sukigara C, Mino Y. 2016. Primary productivity at the time-series stations in the northwestern Pacific Ocean: is the subtropical station unproductive? Journal of Oceanography, 72: 359-371.

Moutin T, Wagener T, Caffin M, Fumenia A, Gimenez A, Baklouti M, Bouruet-Aubertot P, Pujo-Pay M, Leblanc K, Lefevre D, Nunige S H, Leblond N, Grosso O, de Verneil A. 2018. Nutrient availability and the ultimate control of the biological carbon pump in the western tropical South Pacific Ocean. Biogeosciences, 15: 2961–2989.

Murphy S C, Nazzaro L J, Simkins J, Oliver M J, Kohut J, Crowley M, Miles T N. 2021. Persistent upwelling in the Mid-Atlantic Bight detected using gap-filled, high-resolution satellite SST. Remote Sensing of Environment, 262: 112487.

Nowicki M, DeVries T, Siegel D A. 2022. Quantifying the carbon export and sequestration pathways of the ocean's biological carbon pump. Global Biogeochemical Cycles, 36(3): e2021GB007083.

O'Connor B M, Fine R A, Maillet K A, Olson D B. 2002. Formation rates of subtropical underwater in the Pacific Ocean. Deep-Sea Research I, 49(9): 1571-1590.

Panaïotis, T., Poteau, A., Riquier, É. D., Catalano, C., Courchet, L., Motreuil, S., Coppola, L., Picheral, M., Irisson, J. O.: Temporal evolution of plankton and particles distribution across a mesoscale front during the spring bloom. Limnol. Oceanogr., 9999, 1–15, https://doi.org/10.1002/lno.12566, 2024.

Parsons T R, Maita Y, Lalli C M. 1984. A manual of chemical and biological methods for seawater analysis. New York, NY: Pergamon, 173.

Pennington J T, Mahoney K L, Kuwahara V S, Kolber D D, Calienes R, Chavez F P. 2006. Primary production in the eastern tropical Pacific: A review. Progress in Oceanography, 69: 285-317.

Picheral, M., Guidi, L., Stemmann, L., Karl, D. M., Iddaoud, G., Gorsky, G.: The Underwater Vision Profiler 5: an advanced instrument for high spatial resolution studies of particle size spectra and zooplankton. Limnol. Oceanogr-Meth., 8, 462–473, https://doi.org/10.4319/lom.2010.8.462, 2010.

Qin, X. W., Luo, W. D., Li, P. F., Chen, H. J., Xiao, X., Hu, G., Tan, Y. F., Du, R. L., Sun, M. J., Cong, J. Y., Hu, X. S., Lu, K., Wang, L. X., Zhang, H. D., Zhou, H. Y.: Topographic and geomorphological features and tectogenesis of the southern section of the Kyushu-Palau Ridge (KPR) and its adjacent areas. China Geology, 4, 571–584, https://doi.org/10.31035/cg2021076, 2021.

Ramondenc, S., Madeleine, G., Lombard, F., Santinelli, C., Stemmann, L., Gorsky, G., Guidi, L.: An initial carbon export assessment in the Mediterranean Sea based on drifting sediment traps and the underwater vision profiler data sets. Deep-Sea Res. PT I, 117, 107–119, https://doi.org/10.1016/j.dsr.2016.08.015, 2016.

Ramondenc, S., Eveillard, D., Metfies, K., Iversen, M. H., Nöthig, E. M., Piepenburg, D., Hasemann, C., Soltwedel, T.: Unveiling pelagic-benthic coupling associated with the biological carbon pump in the Fram Strait

© Author(s) 2026. CC BY 4.0 License.

(Arctic Ocean). Nature Communications, 16, 840, https://doi.org/10.1038/s41467-024-55221-x, 2025.
Richardson, T. L., Jackson, G. A.: Small phytoplankton and carbon export from the surface ocean. Science, 315, 838–840, DOI: 10.1126/science.1133471, 2007.
Riley, J. S., Sanders, R., Marsay, C., Le Moigne, F. C., Achterberg, E. P., Poulton, J.: The relative contribution of fast and slow sinking particles to ocean carbon export. Global Biogeochem. Cycles, 26, 1–10, https://doi.org/10.1029/2011GB004085, 2012.
Rodil, I. F., Lucena-Moya, P., Tamelander, T., Norkko, J., Norkko, A.: Seasonal variability in benthic–pelagic coupling: quantifying organic matter inputs to the seafloor and benthic macrofauna using a multi-marker approach. Frontiers in Marine Science, 7, 404, https://doi.org/10.3389/fmars.2020.00404, 2020.
Rowler, D. B., Forte, A. M., Rowan, C. J., Glišović, M. R., Grand, S. P., Simmons, N. A.: Kinematics and dynamics of the East Pacific Rise linked to a stable, deep-mantle upwelling. Science Advances, 2, e1601107, 10.1126/sciadv.160110, 2016.
Schofield, O., Brown, M., Kohut, J., Nardelli, S., Saba, G., Waite, N., Ducklow, H.: Changes in the upper ocean mixed layer and phytoplankton productivity along the West Antarctic Peninsula. Philosophical Transactions of the Royal Society A, 376(2122), 20170173, https://doi.org/10.1098/rsta.2017.0173, 2018.
Searle, R.: Mid-ocean ridges. Cambridge University Press, Cambridge (318 pp.), 2013.
Seo, J., Kim, G., Park, J. H., Seo, H., Na, T., Kang, S. K., Hwang, J.: Export of particulate organic carbon (POC) in the eddy region of the tropical northwest Pacific. Frontiers in Marine Science, 9, 976201, https://doi.org/10.3389/fmars.2022.976201, 2022.
Shih, Y. Y., Hung, C. C., Gong, G. C., Chung, W. C., Wang, Y. H., Lee, I. H., Chen, K. S., Ho, C. Y.: Enhanced particulate organic carbon export at eddy edges in the oligotrophic Western North Pacific Ocean. Plos One, 10(7), e0131538, https://doi.org/10.1371/journal.pone.0131538, 2015.
Siegel, D. A., DeVries, T., Cetinić Bisson, K. M.: Quantifying the ocean's biological pump and its carbon cycle impacts on global scales. Annual Review of Marine Science, 15, 329–356, https://doi.org/10.1146/annurev-marine-040722-115226, 2023.
Song, Q. F., Zhou, C., Xiao, X., Xun, H., Tian, Z. C., Yang, Q. X., Zhao, W., Tian, J. W.: Spatial and temporal variability of turbulent mixing in the deep Northwestern Pacific. Journal of Geophysical Research, 129, e2023JC020864, https://doi.org/10.1029/2023JC020864, 2024.
Stamieszkin, K., Poulton, N. J., Pershing, A. J.: Zooplankton grazing and egestion shifts particle size distribution in natural communities. Marine Ecology Progress Series, 575, 43–56, https://doi.org/10.3354/meps, 2017.
Stemmann, L., Eloire, D., Sciandra, A., Jackson, G. A., Guidi, L., Picheral, M., Gorsky, G.: Volume distribution for particles between 3.5 to 2000 µm in the upper 200 m region of the South Pacific Gyre. Biogeosciences, 5, 299–310, https://doi.org/10.5194/bg-5-299-2008, 2008.
Turner, J. T.: Zooplankton fecal pellets, marine snow, phytodetritus and the ocean's biological pump. Progress in Oceanography, 130, 205–248, https://doi.org/10.1016/j.pocean.2014.08.005, 2015.
Turner, J. S., Pretty, J. L., McDonnell, A. M. P.: Marine particles in the Gulf of Alaska shelf system: Spatial patterns and size distributions from in situ optics. Cont. Shelf Res., 145, 13–20, https://doi.org/10.1016/j.csr.2017.07.002, 2017.
Ueno, H., Bracco, A., Barth, J. A., Budyansky, M. V., Hasegawa, D., Itoh, S., Kim, S. Y., Ladd, C., Lin, X. P., Park, Y. G., Prants, S., Ross, T., Rypina, I. I., Sasai, Y., Trusenkova, O. O., Ustinova, E. I., Zhong, Y. S.: Review

© Author(s) 2026. CC BY 4.0 License.

of oceanic mesoscale processes in the North Pacific: Physical and biogeochemical impacts. Progress in Oceanography, 212, 102955, https://doi.org/10.1016/j.pocean.2022.102955, 2023.

Van Ruth, P. D., Ganf, G. G., Ward, T. M.: The influence of mixing on primary productivity: A unique application of classical critical depth theory. Progress in Oceanography, 85(3–4), 224–235, https://doi.org/10.1016/j.pocean.2010.03.002, 2010.

Vinayachandran, P. N. M., Masumoto, Y., Roberts, M. J., Huggett, J. A., Halo, I., Chatterjee, A., Amol, P., Gupta, G. V. M., Singh, A., Mukherjee, A., Prakash, S., Beckley, L. E., Raes, E. J., Hood, R.: Reviews and syntheses: Physical and biogeochemical processes associated with upwelling in the Indian Ocean. Biogeosciences, 18(22), 5967–6029, https://doi.org/10.5194/bg-18-5967-2021, 2021.

Visser, A. W.: Sequestration by the biological carbon pump: Do we really know what we are talking about? Limnology and Oceanography Letters, 10(6), 851–858, 10.1002/lol2.70053, 2025.

Wang, W. L., Fu, W. W., Le Moigne, F. A. C., Letscher, R. T., Liu, Y., Tang, J. M., Primeau, F. W.: Biological carbon pump estimate based on multidecadal hydrographic data. Nature, 624, 579–585, https://doi.org/10.1038/s41586-023-06772-4, 2023a.

Wang, X. X., Liu, Z. F., Li, J. Y., Lin, B. Z., Zhao, Y. L., Zhang, X. D., Cao, J. Y., Zhang, J. W., Song, H. Z., Wang, W. Z.: Sinking fate and carbon export of zooplankton fecal pellets: insights from time-series sediment trap observations in the northern South China Sea. Biogeosciences, 20, 5109–5123, https://doi.org/10.5194/bg-20-5109-2023, 2023b.

Wang, X. Y., Li, H. L., Zhang, J. J., Chen, J. F., Xie, X. H., Xie, W., Yin, K. D., Zhang, D. S., Ruiz-Pino, D., Kao, S. J.: Seamounts generate efficient active transport loops to nourish the twilight ecosystem. Sci. Adv., 10(26), eadk6833, 10.1126/sciadv.adk68, 2024a.

Wang, Z. Y., Fang, C., Yang, C. H., Zhang, G. Y., Sun, D.: Latitudinal gradient and influencing factors of deep-sea particle export along the Kyushu-Palau Ridge in the Philippine Sea. Sci. Total Environ., 906, 167460, https://doi.org/10.1016/j.scitotenv.2023.167460, 2024b.

Whitney, F. A., Crawford, W. R., Harrison, P. J.: Physical processes that enhance nutrient transport and primary productivity in the coastal and open ocean of the subarctic NE Pacific. Deep-Sea Research II, 52, 681–706, https://doi.org/10.1016/j.dsr2.2004.12.023, 2005.

Xiao, X., Zhou, C., Yang, Q. X., Jing, Z. Y., Liu, Z. Y., Yuan, D. L., Xu, Z. H., Zhao, W., Tian, J. W.: Diapycnal upwelling over the Kyushu-Palau Ridge in the North Pacific Ocean. Geophysical Research Letters, 50, e2023GL104369, https://doi.org/10.1029/2023GL104369, 2023.

Xu, Z. C., Zheng, Z. Q., Xu, C., Xu, F. P., Chen, J. X., Liu, X., Landry, M. R., Huang, B. Q.: Primary production drives varied zooplankton migration strength and twilight-zone particle dynamics across ecological gradients in the western North Pacific. Limnology and Oceanography, 70, 1621–1635, https://doi.org/10.1002/lno.70074, 2025.

Zapata, M., Rodríguez, F., Garrido, J.: Separation of chlorophylls and carotenoids from marine phytoplankton: a new HPLC method using a reversed phase C8 column and pyridine-containing mobile phases. Marine Ecology Progress Series, 195, 29–45, https://www.jstor.org/stable/24855008, 2000.

Zhang, G. C., Liu, Z. S., Zhang, Z. Y., Ding, C. L., Sun, J.: The impact of environmental factors on the phytoplankton communities in the Western Pacific Ocean: HPLC-CHEMTAX approach. Frontiers in Marine Science, 10, 1185939, https://doi.org/10.3389/fmars.2023.1185939, 2023.

Zhong, Q. Q., Yu, T., Lin, H., Lin, J., Ji, J. D., Ni, J. L., Du, J. Z., Huang, D. K.: ^{210}Po-^{210}Pb disequilibrium in the

https://doi.org/10.5194/egusphere-2026-597
Preprint. Discussion started: 23 February 2026
© Author(s) 2026. CC BY 4.0 License.

western North Pacific Ocean: particle cycling and POC export. Frontiers in Marine Science, 8, 700524, https://doi.org/10.3389/fmars.2021.700524, 2021.

Zhou, C., Xu, H., Xiao, X., Zhao, W., Yang, J., Yang, Q., Jiang, H., Xie, Q., Long, T., Wang, T., Huang, X., Zhang, Z., Guan, S., Tian, J.: Intense abyssal flow through the Yap-Mariana Junction in the Western North Pacific. Geophysical Research Letters, 49(3), e2021GL096530, https://doi.org/10.1029/2021GL096530, 2022.